

DOI: 10.1002/adfm.200800306

# Theoretical and Experimental Studies of Bending of Inorganic Electronic Materials on Plastic Substrates\*\*

By Sang-Il Park, Jong-Hyun Ahn, Xue Feng,\* Shuodao Wang, Yonggang Huang, and John A. Rogers\*

This paper describes materials and mechanics aspects of bending in systems consisting of ribbons and bars of single crystalline silicon supported by sheets of plastic. The combined experimental and theoretical results provide an understanding for the essential behaviors and for mechanisms associated with layouts that achieve maximum bendability. Examples of highly bendable silicon devices on plastic illustrate some of these concepts. Although the studies presented here focus on ribbons and bars of silicon, the same basic considerations apply to other implementations of inorganic materials on plastic substrates, ranging from amorphous or polycrystalline thin films, to collections of nanowires and nanoparticles. The contents are, as a result, relevant to the growing community of researchers interested in the use of inorganic materials in flexible electronics.

## 1. Introduction

Large-area electronics, sometimes referred to as macro-electronics, has attracted increasing interest in the last decade due to its importance in established systems such as liquid-crystal displays (LCDs) and organic light emitting diode displays (OLEDs). More recently, this class of electronics is being examined for other, new application possibilities that derive from the ability to distribute electronic functionality over sizes that are much larger than those associated with semiconductor wafers.<sup>[1]</sup> For many of these systems, thin and lightweight sheets of plastic represent ideal substrates. Various prototype flexible electronic devices of this type, from paperlike displays<sup>[2]</sup> to sensor skins,<sup>[3]</sup> have been demonstrated, most commonly by use of semiconductors based on small molecule or polymer organics.<sup>[4–6]</sup> These classes of materials are generally believed to be well suited for these applications because they are themselves considered, in a very loose sense, to be ‘flexible’ and naturally compatible with plastic substrates. Their main disadvantage is that the electrical properties of devices formed with them, such as the effective mobilities observed in thin film transistors, are modest and much worse than those that can be achieved, for example, established inorganic materials. This consideration, combined with the uncertain reliability of the organics, has recently led to interest in the possibility of inorganic based flexible electronics,<sup>[7–13]</sup> in which only the substrates or other passive elements (e.g., dielectrics) are organic. The most basic realization uses thin films of the inorganics as semiconductors, conductors and/or insulators on substrates that are also thin, to minimize the strains induced by bending.<sup>[14,15]</sup> In such designs, it is possible to achieve bend radii of  $\sim 1$  cm and less,<sup>[16]</sup> with plastic substrates that have thicknesses in the 25–150  $\mu\text{m}$  range, even without advanced designs that use concepts of neutral mechanical planes<sup>[17–19]</sup> or buckled material configurations.<sup>[20]</sup> In these simple systems, one often approximates the strains at the circuit level (i.e., at the top surface of the device substrate)

[\*] Prof. J. A. Rogers, S.-I. Park  
Department of Materials Science and Engineering  
Beckman Institute for Advanced Science and Technology  
and Frederick Seitz Materials Research Laboratory  
University of Illinois at Urbana-Champaign  
Urbana, Illinois 61801 (USA)  
E-mail: jrogers@uiuc.edu

Prof. J. A. Rogers  
Department of Chemistry  
Department of Mechanical Science and Engineering  
Department of Electrical and Computer Engineering  
University of Illinois at Urbana-Champaign  
Urbana, Illinois 61801 (USA)

Prof. J.-H. Ahn  
School of Advanced Materials Science and Engineering  
SKKU Advanced Institute of Nanotechnology,  
Sungkyunkwan University  
Suwon, 440-746 (Korea)

Prof. X. Feng  
Department of Engineering Mechanics, Tsinghua University  
Beijing 100084 (P. R. China)  
E-mail: fengxue@tsinghua.edu.cn

S. Wang, Prof. Y. Huang  
Department of Mechanical Engineering, Northwestern University  
Evanston, IL 60208 (USA)

Prof. Y. Huang  
Department of Civil and Environmental Engineering  
Northwestern University  
Evanston, IL 60208 (USA)

[\*\*] We thank T. Banks, K. Colravy, and S. J. Robinson for help with processing. The materials parts of this effort were supported by the U.S. Department of Energy (DoE), Division of Materials Sciences under award no. DE-FG02-07ER46471, through the Materials Research Laboratory (MRL). The general characterization facilities were provided through the MRL with support from the University of Illinois and from DoE grants DE-FG02-07ER46453 and DE-FG02-07ER46471. The mechanics theory and the transfer printing systems were developed under support by the Center for Nanoscale Chemical Electrical Mechanical Manufacturing Systems at the University of Illinois (funded by the NSF under grant DMI-0328162). S.-I. Park would like to thank Samsung SDI for the doctoral fellowship support.

as the ratio of the substrate thickness to twice the bend radius. The degree of bendability is then defined by the bend radius at which the strain reaches some substantial fraction of a fracture strain in a typical inorganic film (e.g., ~1%). This analysis provides some basic guidance but it is far too simple to provide either an accurate description of the mechanics or a predictive framework for understanding different modes of bending induced failure that can occur in these structures.<sup>[21]</sup>

In this paper, we report comprehensive experimental and theoretical studies of bending in structures relevant to inorganic flexible electronics. Different from previous mechanics models of related systems,<sup>[21]</sup> our analysis does not assume the thin film to cover the entire substrate, thereby explicitly accounting for effects of edges and finite device sizes, both of which play critically important roles in the mechanics and bending properties. These thin-film islands give non-uniform stress, with maxima that often appear at the edges and spatially non-uniform shear and normal stresses along the film/substrate interface. Although these results are generally applicable to all classes of flexible inorganic electronics, the experiments focus on systems that integrate thin membranes and ribbons of single crystalline silicon, in various configurations, on plastic substrates of different types. The observations and analysis explain all of the different failure mechanisms in unoptimized systems; they also rationalize the key mechanisms by which somewhat more advanced layouts can achieve enhanced robustness on bending. Implementation of these concepts to achieve highly bendable arrays of silicon p-n junction diodes on plastic demonstrates these results in practical devices.

## 2. Results and Discussion

### 2.1. Fabrication of Si Ribbons on Plastic Substrates

Figure 1 schematically illustrates the processing steps for creating and transferring thin ribbons of silicon from a source wafer to a plastic substrate and the types of bending tests that were performed. The layouts were designed explicitly to reveal the key aspects of the mechanics and the various possible failure modes. They are not intended for practical use in flexible electronics; subsequent sections describe multilayer structures that are more suitable for this purpose. The first step involved the definition of Si ribbons from a silicon-on-insulator (SOI) wafer, using SF<sub>6</sub> reactive ion etching (RIE) through a patterned layer of photoresist. In the case of thick (i.e., 10 μm) Si, etching was performed with a SF<sub>6</sub>/O<sub>2</sub> inductively coupled plasma reactive ion etching system (ICPRIE)<sup>[22]</sup> through a pattern layer of hard mask (Si<sub>3</sub>N<sub>4</sub>/SiO<sub>2</sub>, 3/30 nm). Removal of the resist layers followed by undercut etching of the buried oxide with concentrated hydrofluoric acid solution (~49 wt % in water) released arrays of Si ribbons, without physically lifting them off of the wafer. In the next step, contacting a flat elastomeric stamp of polydimethylsiloxane (PDMS) with the Si ribbons and then peeling back the stamp removed the ribbons

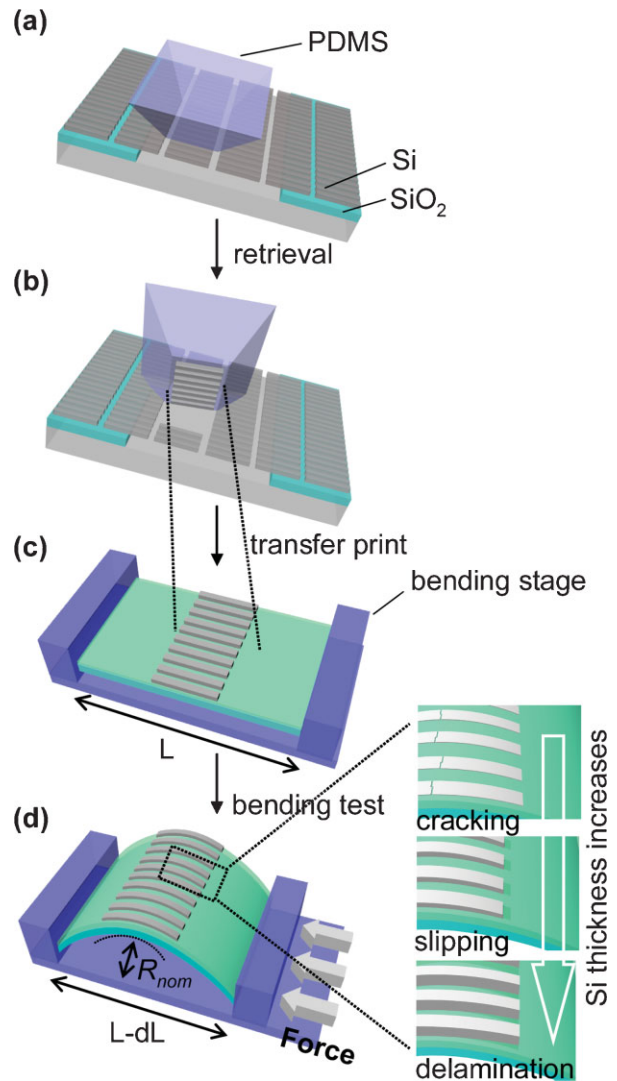


**Figure 1.** Schematic illustration of the steps a)–c) used to transfer-print Si ribbons from a silicon-on-insulator wafer to a plastic substrate coated with adhesive layer and d) the apparatus to evaluate the bending properties. At sufficiently large degrees of bending, various failure mechanisms (i.e., cracking, slipping, or delamination of the ribbons) can be observed, depending on the ribbon thickness, as shown on the right side of d).

from the wafer and left them adhered by van der Waals interactions to the PDMS (Fig. 1a). Efficient transfer of the ribbons from the substrate to the PDMS was accomplished by peeling back the stamp at a relatively high speed (Fig. 1b).<sup>[23]</sup> Contacting the stamp, coated with ribbons in this manner, against a poly(ethyleneterephthalate) (PET) (50 μm or 175 μm thick) substrate coated with a thin epoxy adhesive layer (~1 μm thick) and then removing the stamp completed the transfer process. In all experiments presented here, this epoxy (SU8, Microchem) was spin-coated, soft baked, exposed to UV light and then heated to affect curing on the plastic substrate before the transfer process. Removal of the stamp was performed at slow speeds by use of heating to induce thermal

expansion in the PDMS and, in this way, to initiate separation (Fig. 1c). After the transfer process, the substrate was heated, in a final step, to eliminate the solvent and complete the cure of the epoxy. This configuration results in the ribbons resting on the surface of the epoxy, but neither embedded in it or directly chemically bonded.

## 2.2. Bending Tests

The bending properties, including the failure modes, were investigated using a home-built set of translation stages and fixtures capable of mounting directly in a scanning electron microscope (SEM, at tilted angles and low operating voltages of 1 keV to avoid damage to the sample or other changes induced by heating from the electron beam) for viewing during the bending process. Three different failure modes were observed, depending on the sample type: cracking of the silicon, slipping of the silicon along the interface with the epoxy and delamination of the silicon from the epoxy. Figure 1d schematically illustrates these modes. The extent of bending necessary to induce failure and the mode for failure depend on the thickness and other dimensions of the silicon, the nature of the adhesive and the thickness of the substrate.

The measurements were performed with the ribbons on substrates with initial lengths  $L$ , subject to compression with external force applied through the bending stage (Fig. 1c). Figure 1d shows the plastic substrate bent to an end-to-end length of  $L - dL$  (i.e., horizontal distance from one edge of the bent substrate to the other). The setups allow the length to be measured with an accuracy better than  $\sim 0.1$  mm, and continuous control of  $L - dL$ , in increments of  $\sim 0.1$  mm. The experimentally measured  $L$  and  $L - dL$  can be used to compute the approximate, nominal bend radius ( $R_{\text{nom}}$ ) defined near the center of the length of the substrate. This quantity is given by the reciprocal of the curvature of substrate as computed from the second derivative of the sinusoidal curve that describes the bent shape  $w = w_0 \sin(\pi X/L)$ , where

$$w_0 = \frac{2}{\pi} L \sqrt{\frac{dL}{L} - \frac{\pi^2 h_s^2}{12L^2}} \quad (1)$$

and  $dL/L$ ,  $h$ ,  $w$ , and  $w_0$  denote the applied strain, the substrate thickness, the deflection of the substrate in the  $z$  direction, and the deflection of the substrate at the center (i.e.,  $X = L/2$ ), respectively. This analysis applies to the experimental configuration, in which the ends of the substrate are free to rotate upon bending (i.e., they are unclamped). This bend radius, given by

$$R_{\text{nom}} = \frac{L}{2\pi \sqrt{\frac{dL}{L} - \frac{\pi^2 h_s^2}{12L^2}}} \quad (2)$$

is an approximate, global value that does not include the mechanical effects of the silicon. We also define a corresponding, nominal bending strain,  $\varepsilon_{\text{nom}}$ , as  $h_s/(2R_{\text{nom}})$ .

## 2.3. Failure Modes: Cracking, Slipping, and Delamination

Figure 2 shows SEM images of silicon ribbons with 100 nm thickness, 20  $\mu\text{m}$  widths and 500  $\mu\text{m}$  lengths on a PET sheet (175  $\mu\text{m}$  thick) with length  $L = 11.8$  mm, coated with an epoxy adhesive layer (1  $\mu\text{m}$  thick). These images show that in this system, as well as the others used to illustrate the mechanics concepts, the silicon rests primarily on the top surface of the adhesive, yielding a configuration that is not well suited to strong bonding to the substrate. As mentioned previously, we chose to study this type of layout because it reveals clearly all of the relevant mechanical behaviors and failure modes. The left insets schematically illustrate the bending geometries. The results show that bending induced failure in this case occurs when cracks appear in the silicon. Cracks are first visible at  $dL/L = 42.4\%$  ( $R_{\text{nom}} \sim 2.88$  mm,  $\varepsilon_{\text{nom}} \sim 3.04\%$ ). The cracks form near the centers of the ribbons, and originate from single fracture lines that run across the ribbons and propagate through different paths resulting in many fractured pieces at values of strain ( $dL/L = 45.8\%$ ) larger than the failure

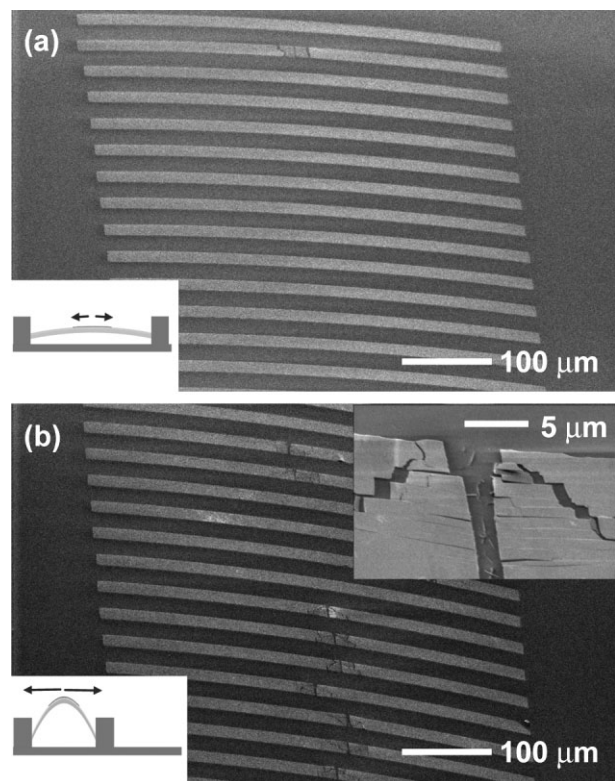


**Figure 2.** SEM images of bending in thin Si ribbons (thickness = 100 nm, width = 20  $\mu\text{m}$ , length = 500  $\mu\text{m}$ ) on an epoxy ( $\sim 1$   $\mu\text{m}$ )/PET (175  $\mu\text{m}$ ) substrate, corresponding to a)  $dL/L = 35.6\%$  ( $R_{\text{nom}} \sim 3.15$  mm,  $\varepsilon_{\text{nom}} \sim 2.78\%$ ) and b)  $dL/L = 45.8\%$  ( $R_{\text{nom}} \sim 2.78$  mm,  $\varepsilon_{\text{nom}} \sim 3.15\%$ ). The critical point for this cracking failure more is  $dL/L \sim 42.4\%$  ( $R_{\text{nom}} \sim 2.88$  mm,  $\varepsilon_{\text{nom}} \sim 3.04\%$ ). The bottom left insets provide schematic illustrations of the bending geometries. The upper right inset of b) shows a magnified view of the cracking.

threshold (Fig. 2b). The right inset of Figure 2b provides a magnified view of a cracked region.

As expected, the thickness of the ribbons plays an important role in the mechanics. To illustrate the effects, Figure 3 shows SEM images of the edges of silicon ribbons with 700 nm thicknesses in designs that are otherwise similar to those of Figure 2, except that a 50  $\mu\text{m}$  thick PET substrate ( $L = 11.8 \text{ mm}$ ) was used to achieve  $dL/L$  values at failure that are convenient for measurement. In this case, instead of cracking, we observed that the ribbons slip on the substrate at  $dL/L = 9.0\%$  ( $R_{\text{nom}} \sim 6.26 \text{ mm}$ ,  $\varepsilon_{\text{nom}} \sim 0.40\%$ ), as shown in Figure 3a. Figure 3a–c shows that the Si ribbons slip by

progressively increasing amounts as  $dL/L$  increases [a) 9.0%, b) 31.4%, and c) 50.8%]. This slipping reduces the strain in the silicon, thereby preventing the cracking failure mode even at extremely high values of  $dL/L$ . As the bending is released, the silicon ribbons often do not slip back to their original locations but instead buckle upward via local delamination from the adhesive, in a manner that foreshadows the third failure mode. This slipping result shows clearly an example of a system in which degree of bendability is not determined simply by the fracture strains of inorganic electronic materials. Instead, interfacial shear stresses ( $\tau$ ), which are responsible for the slipping behavior, determine failure. These shear stresses have maximum values near the free edges of the silicon. Unlike fracture, which is limited by the failure strain of the silicon, this failure mode is extremely sensitive to the strength of adhesive bonding to the substrate.

Increasing the silicon thickness further reveals additional failure modes. Figure 4 shows SEM images for the case of 2.5  $\mu\text{m}$  thickness, with other parameters the same as those in Figure 3. Here, bending induces some slipping, first observed at

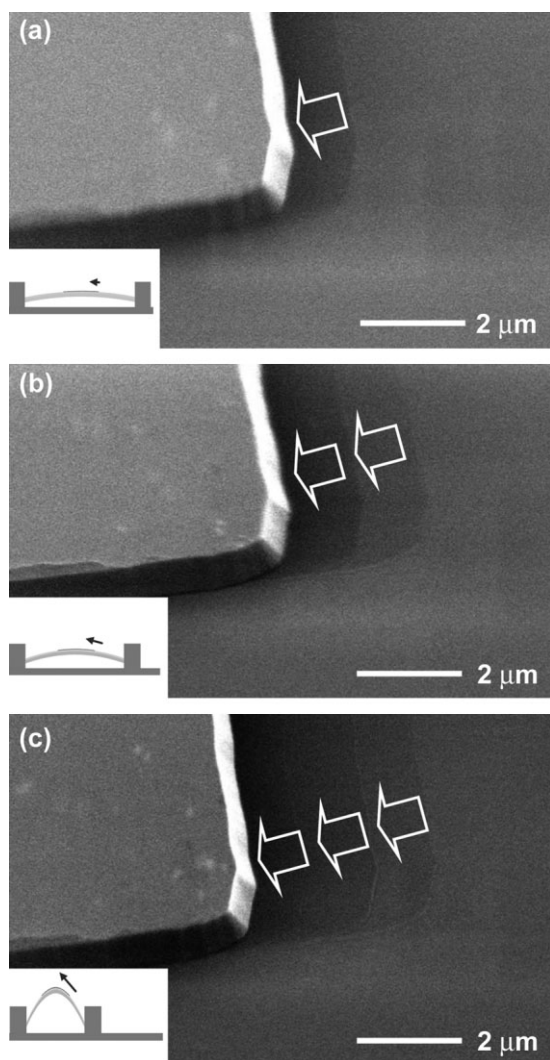


**Figure 3.** SEM images of bending in thin Si ribbons (thickness = 700 nm, width = 20  $\mu\text{m}$ , length = 500  $\mu\text{m}$ ) on an epoxy ( $\sim 1 \mu\text{m}$ )/PET (50  $\mu\text{m}$ ) substrate, corresponding to a)  $dL/L = 9.0\%$  ( $R_{\text{nom}} \sim 6.26 \text{ mm}$ ,  $\varepsilon_{\text{nom}} \sim 0.40\%$ ), b)  $dL/L = 31.4\%$  ( $R_{\text{nom}} \sim 3.35 \text{ mm}$ ,  $\varepsilon_{\text{nom}} \sim 0.75\%$ ) and c)  $dL/L = 50.8\%$  ( $R_{\text{nom}} \sim 2.63 \text{ mm}$ ,  $\varepsilon_{\text{nom}} \sim 0.95\%$ ). The bottom left insets provide schematic illustrations of the bending geometries. These images reveal the progression of the slipping failure mode. Slipping begins at approximately  $dL/L \sim 9.0\%$ .

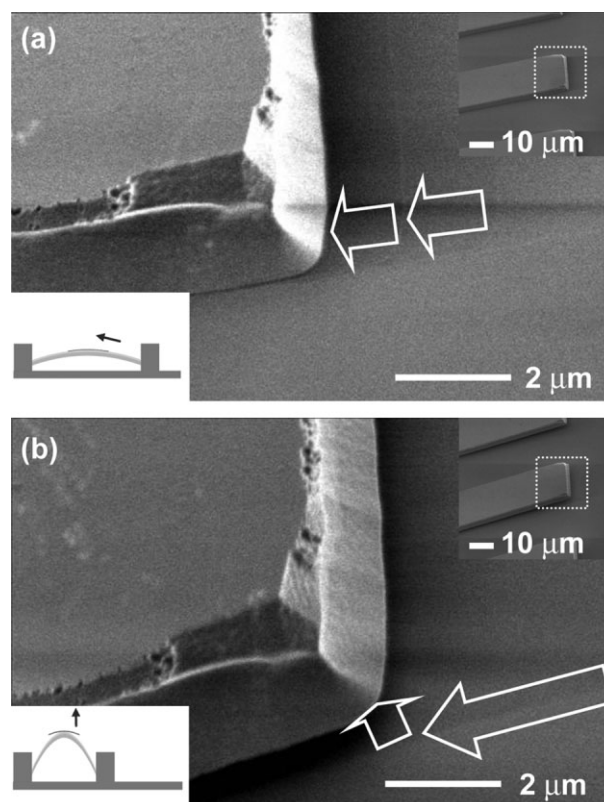


**Figure 4.** SEM images of bending in thin Si ribbons (thickness = 2.5  $\mu\text{m}$ , width = 20  $\mu\text{m}$ , length = 500  $\mu\text{m}$ ) on an epoxy ( $\sim 1 \mu\text{m}$ )/PET (50  $\mu\text{m}$ ) substrate, corresponding to a)  $dL/L = 3.4\%$  ( $R_{\text{nom}} \sim 10.2 \text{ mm}$ ,  $\varepsilon_{\text{nom}} \sim 0.25\%$ ), b)  $dL/L = 53.4\%$  ( $R_{\text{nom}} \sim 2.57 \text{ mm}$ ,  $\varepsilon_{\text{nom}} \sim 0.97\%$ ). The bottom left and upper right insets provide schematic illustrations of the bending geometries and low magnification SEM images, respectively. These images reveal a failure mechanism that involves first slipping a) followed by delamination b).

$dL/L = 3.4\%$ , ( $R_{\text{nom}} \sim 10.2 \text{ mm}$ ,  $\varepsilon_{\text{nom}} \sim 0.25\%$ ), as shown in Figure 4a. As the applied strain ( $dL/L$ ) increases to much higher values of 53.4% ( $R_{\text{nom}} \sim 2.6 \text{ mm}$ ,  $\varepsilon_{\text{nom}} \sim 0.98\%$ ), the silicon is observed to delaminate from the substrate, as shown in Figure 4b. This third failure mode is driven by interface normal stresses ( $\sigma$ ), i.e., peeling stresses. At even larger Si thicknesses, this delamination is observed without slipping. Figure 5a–c presents results for 10  $\mu\text{m}$  thickness, with other

parameters the same as those in Figure 4, except that  $L = 11.7 \text{ mm}$ . Here, delamination begins at  $dL/L = 2.6\%$  ( $R_{\text{nom}} \sim 11.6 \text{ mm}$ ,  $\varepsilon_{\text{nom}} \sim 0.22\%$ ) as shown in Figure 5a. The delamination initiates at the edges of the ribbons, and then propagates to the center as the bending increases (Fig. 5b and c). Removing the bending forces relaxes the system back to its initial flat state, without the sort of buckling that can be observed when slipping occurs.

Many similar considerations apply, in a qualitative sense, to the case of inward bending, which leads to compressive, rather than tensile, strains and stresses near the silicon. Figure 6 shows SEM images for the cases of ribbons with 700 nm and 10  $\mu\text{m}$  thicknesses, and other parameters the same as those in Figure 5 except that  $L = 11.8 \text{ mm}$ , after inward bending beyond the failure mode and then relaxing. In the case of 700 nm thickness, evidence of slipping was observed on the adhesive layer after relaxing from inward bending corresponding to  $dL/L = 29.7\%$  ( $R_{\text{nom}} \sim 3.45 \text{ mm}$ ,  $\varepsilon_{\text{nom}} \sim 0.73\%$ ) as shown in Figure 6a. The inset of Figure 6a shows that no such marks of slipping could be observed while in the bent condition ( $dL/L = 29.7\%$ ), due to the direction of the slipping in this case. In other words, marks of slipping are hidden beneath the silicon in this configuration. Figure 6b presents, in the same manner, results for ribbons with 10  $\mu\text{m}$  thickness. The slipping marks were observed after relaxing from inward bending of  $dL/L = 19.5\%$  ( $R_{\text{nom}} \sim 4.25 \text{ mm}$ ,  $\varepsilon_{\text{nom}} \sim 0.59\%$ ). Practical considerations in imaging make it difficult to determine whether the delamination mode is present in these cases. Theoretical considerations, described in a subsequent section, can address this issue.

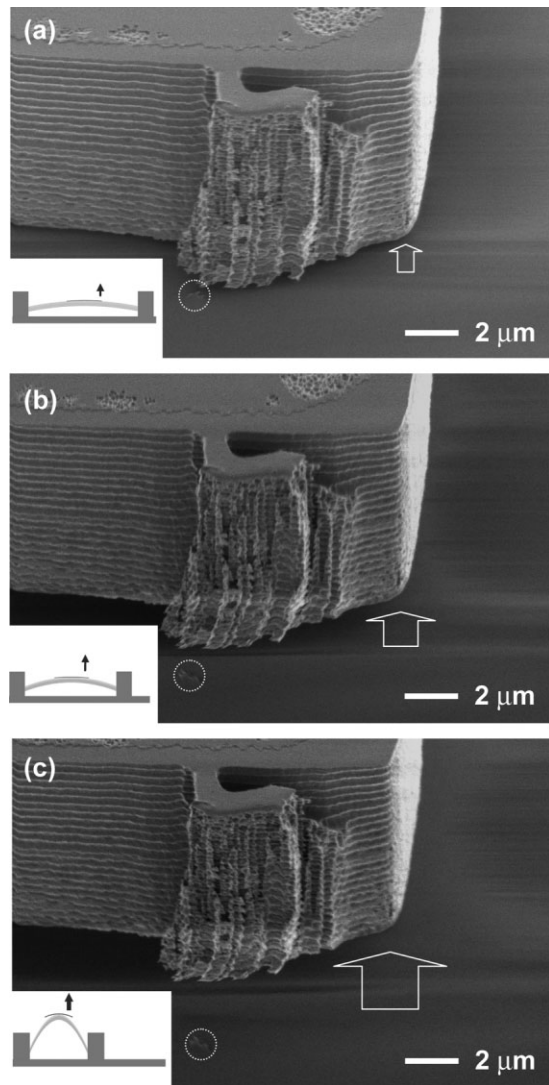


**Figure 5.** SEM images of bending in thin Si ribbons (thickness = 10  $\mu\text{m}$ , width = 20  $\mu\text{m}$ , length = 500  $\mu\text{m}$ ) on an epoxy ( $\sim 1 \mu\text{m}$ )/PET (50  $\mu\text{m}$ ) substrate, corresponding to a)  $dL/L = 2.6\%$  ( $R_{\text{nom}} \sim 11.7 \text{ mm}$ ,  $\varepsilon_{\text{nom}} \sim 0.22\%$ ), b)  $dL/L = 4.3\%$  ( $R_{\text{nom}} \sim 9.06 \text{ mm}$ ,  $\varepsilon_{\text{nom}} \sim 0.28\%$ ), and c)  $dL/L = 6.0\%$  ( $R_{\text{nom}} \sim 7.67 \text{ mm}$ ,  $\varepsilon_{\text{nom}} \sim 0.33\%$ ). The bottom left and upper right insets provide schematic illustrations of the bending geometries and low magnification SEM images, respectively. Delamination begins at about  $dL/L = 2.2\%$  ( $R_{\text{nom}} \sim 12.7 \text{ mm}$ ,  $\varepsilon_{\text{nom}} \sim 0.20\%$ ) and increases with further bending. The fragment indicated by the white circle serves as a marker to track the movement of Si from the substrate. The bottom left insets provide schematic illustrations of the bending geometries.

#### 2.4. Length Effect of the Ribbons

In addition to thickness, the lengths of the ribbons influence the bending mechanics, although direct measurements are difficult due to limited resolution in imaging and the small slip distances associated with the onset of failure. For this reason, as illustrated in Figure 7, we used electrical data from Si ribbon p–n junction diodes to illustrate the importance of ribbon length. The diodes consist of small arrays of ribbons each with thicknesses of 290 nm, doped to high concentration of phosphorous (n-type,  $\sim 10^{19} \text{ cm}^{-3}$ ) on one side and low concentration of boron (p-type,  $6.0\text{--}9.4 \times 10^{14} \text{ cm}^{-3}$ ) on the other, as shown in optical images of Figure 7. The ribbons are placed on a PET substrate (175  $\mu\text{m}$  thick) with an epoxy coating ( $\sim 1 \mu\text{m}$  thick), in a manner similar to that of the test structures described in the previous sections except that  $L = 12.0 \text{ mm}$ . For electrical contacts, ends of the ribbons were patterned with Ti/Au (thickness = 5/70 nm) using procedures described in the experimental section. The current ( $\mu\text{A}/\text{ribbons}$ )–voltage responses of the diodes were determined by making electrical contact to the metal on the plastic substrate near the devices, beyond the ends of the silicon ribbons. Figure 7a presents the current–voltage response of a representative diode that uses

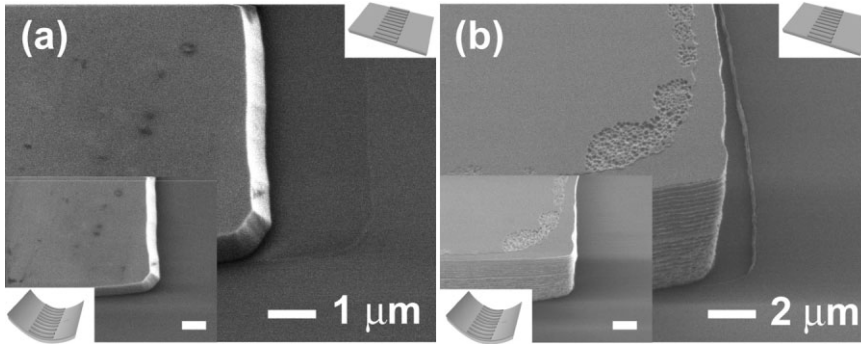


**Figure 6.** SEM images a) of thin Si ribbons (thickness = 700 nm, width = 20 μm, length = 500 μm) on an epoxy (~1 μm)/PET (50 μm) substrate, collected in a flat state after inward bending to  $dL/L = 29.7\%$  ( $R_{nom} \sim 3.45$  mm,  $\epsilon_{nom} \sim 0.73\%$ ) and b) of thin Si ribbons (thickness = 10 μm,  $W/L = 20 \mu\text{m}/500 \mu\text{m}$ ) on an epoxy (~1 μm)/PET (50 μm) substrate, collected in a flat state after inward bending to  $dL/L = 19.5\%$  ( $R_{nom} \sim 4.25$  mm,  $\epsilon_{nom} \sim 0.59\%$ ). The upper right and lower left schematic illustrations show the configuration of the samples for the main frame and lower left inset SEM images, respectively.

long (500 μm) ribbons, evaluated at different degrees of bending. The legend shows the nominal bend radius ( $R_{nom}$ ). With increasing applied strain  $dL/L$  (i.e., decreasing  $R_{nom}$ ), the on-current increases slightly. At the onset of slipping ( $dL/L = 5.0\%$ ;  $R_{nom} \sim 8.56$  mm;  $\epsilon_{nom} \sim 1.02\%$ ), the diode completely ceases to operate, due to loss of electrical contact between the metal probing pads and the silicon associated with fracture of the metal at the silicon edge, as shown in the inset of Figure 7a. In contrast, we observed that for ribbons with lengths of 50 μm (comparable to those useful for real devices, for example), the electrical performance of diode is stable under much higher degrees of bending (i.e., up to  $dL/L \sim 16.0\%$ ;  $R_{nom} \sim 4.78$  mm;  $\epsilon_{nom} \sim 1.83\%$ ) than that of the longer devices as shown in Figure 7b. Moreover, these short devices also show good behavior during mechanical cycling (up to 200 cycles, from the flat state to bending at  $dL/L = 16.0\%$ ) as shown in Figure 7c.

## 2.5. Mechanical Models

All of the observations described in the previous two sections can be understood using analytical models of the bending mechanics. To summarize these results, Table 1 presents the failure modes as a function of Si thickness ( $h_f$ ). Thin Si ribbons (100 nm) on the 175 μm thick PET substrate exhibit the cracking mode, intermediate ribbons (290 nm  $\leq h_f \leq 1.25 \mu\text{m}$ ) on the 50 μm thick PET substrate exhibit slipping (without any cracking) and thick ribbons (10 μm) on the 50 μm thick PET substrate exhibit the delamination mode. Both slipping and delamination are observed, in sequence, with thicknesses in the range of 2.5 μm on a 50 μm thick PET substrate.

We begin with a model based on beam theory, as illustrated in Figure 8. This theory, as described below, can capture all of

the key effects except the length dependence, which is discussed separately. The substrate is modeled as a beam of length  $L$  which is subjected to axial compression (Fig. 8a) to reduce the beam length to  $L - dL$ . Once  $dL/L$  reaches a critical strain  $\pi^2 h_s^2 / 12L^2$ ,<sup>[24]</sup> the substrate bends, where  $h_s$  is the substrate thickness. For parameters characteristic of many of the experimental systems (i.e.,  $L = 11.8$  mm and  $h_s = 50 \mu\text{m}$ ), this critical strain is 0.0015%. As  $dL/L$  continues to increase, the axial compressive force (per unit width of the substrate) remains a constant

$$F = \frac{\pi^2 E'_s h_s^3}{12L^2} \quad [24] \quad (3)$$

where

$$E'_s = \frac{E_s}{1 - \nu_s^2} \quad (4)$$

and  $E_s$  and  $\nu_s$  are the Young's modulus and Poisson's ratio of the substrate. The bending moment in the beam is  $Fw$ , where the lateral displacement takes the form  $w = w_0 \sin(\pi X/L)$ ,  $X = 0$  and  $L$  denote two ends of the beam, and the maximum deflection  $w_0$  is given by Equation 1. This gives the nominal bend radius  $R_{nom}$  around the center as Equation 2. The silicon films are attached to the center of the top substrate surface via the epoxy adhesive layer (Fig. 8a). The film thickness  $h_f$  and adhesive layer thickness  $h_a$  are much smaller than the substrate thickness,  $h_f, h_a \ll h_s$ , but the elastic modulus of silicon  $E'_f$  is much larger than its counterparts  $E'_s$  and  $E'_a$  of the PET substrate and epoxy adhesive layer, respectively,  $E'_f \gg E'_s, E'_a$ . Therefore, the bending stiffness of the adhesive layer is much smaller than those of the films and substrate,  $E'_a h_a \ll E'_f h_f, E'_s h_s$ .

Figure 8b shows the system composed of a thin film, adhesive layer and substrate subjected to the axial compressive force  $F$  and bending moment  $M = F w_0$  (per unit width of the substrate). The film and substrate are modeled as beams, while a shear lag model is used for the adhesive layer due to its low stiffness. Jiang et al. (1997) and Wang et al. (2000) obtained the analytic solution for this problem. The surface strain of the silicon film and the nominal bending strain  $\epsilon_{nom}$ , defined by  $h_s / (2R_{nom})$ , are shown versus the applied strain  $dL/L$  in Figure 9a and b, respectively, for the 100 nm thick Si ribbons, 1 μm thick epoxy adhesive layer and 175 μm thick PET substrate. The surface strain of the film is much smaller than the nominal bending strain  $\epsilon_{nom}$  because the adhesive layer relaxes the stretch transmitted from the substrate to the film.

The shear and peeling stresses along the film/adhesive interface reach a maximum at the tip (edge) of the film, and are responsible for the slip and delamination of interface,

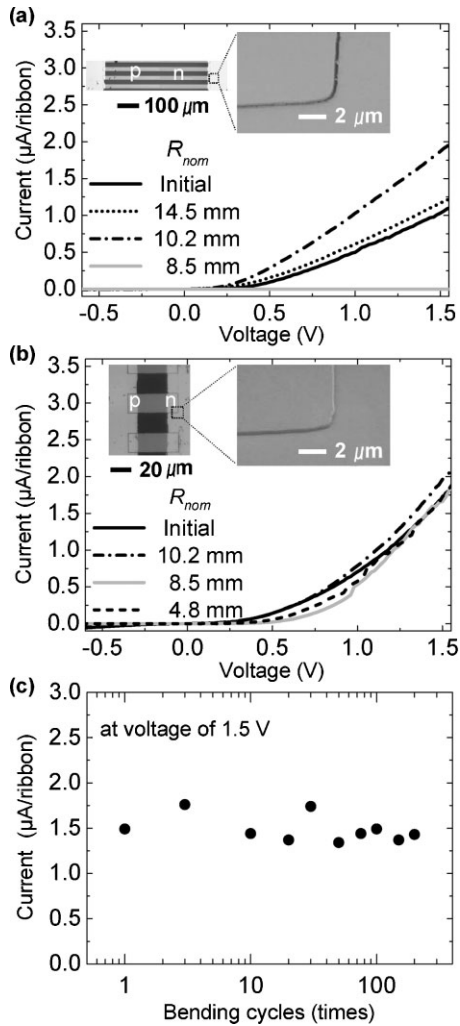


**Figure 7.** Electrical properties of diodes consisting of doped silicon ribbons with lengths of a) 500  $\mu\text{m}$  and b) 50  $\mu\text{m}$  under externally applied strain  $dL/L$ . The data correspond to current normalized to a single ribbon. a) The diode using long Si ribbons (500  $\mu\text{m}$ ) does not operate at  $dL/L = 5.0\%$  ( $R_{\text{nom}} \sim 8.56 \text{ mm}$ ,  $\varepsilon_{\text{nom}} \sim 1.02\%$ ), but b) that using short Si ribbons (50  $\mu\text{m}$ ) operates even at higher applied strain of 16.0% ( $R_{\text{nom}} \sim 4.78 \text{ mm}$ ,  $\varepsilon_{\text{nom}} \sim 1.83\%$ ). c) Current at 1.5 V and  $dL/L = 16.0\%$  as a function of bending cycles, i.e., after bending (to 16.0% strain) and unbending devices several hundred times. For both sets of devices, the Si ribbons (thickness = 290 nm, width = 20  $\mu\text{m}$ ) are on an epoxy ( $\sim 1 \mu\text{m}$ )/PET (175  $\mu\text{m}$ ) substrate.

respectively. The maximum shear stress is given by<sup>[25,26]</sup>

$$\tau_{\text{max}} = \frac{\pi G_a h_s}{\lambda h_a L} \sqrt{\frac{dL}{L} - \frac{\pi^2 h_s^2}{12L^2}} \quad (5)$$

where  $G_a$  is the shear modulus of the adhesive layer and

$$\lambda = 2 \sqrt{\frac{G_a}{h_a} \left( \frac{1}{E_f' h_f} + \frac{1}{E_s' h_s} \right)} \quad (6)$$

The maximum peeling stress along the film/adhesive interface is given by<sup>[25,26]</sup>

$$\sigma_{\text{max}} = \left[ \beta G_a h_s \left( \frac{2\chi^3}{\lambda^2} + \frac{\lambda}{2} - \frac{\chi^2}{\lambda} \right) + E_a' \right] \frac{\pi}{\chi^2 h_a L} \sqrt{\frac{dL}{L} - \frac{\pi^2 h_s^2}{12L^2}} \quad (7)$$

where

$$\chi = \left[ 3 \frac{E_a'}{h_a} \left( \frac{1}{E_f' h_f^2} + \frac{1}{E_s' h_s^2} \right) \right]^{\frac{1}{4}} \quad (8)$$

$$\beta = \frac{3 \left( \frac{1}{E_f' h_f^2} - \frac{1}{E_s' h_s^2} \right) \frac{h_a}{G_a} \lambda}{4(1 - \nu_a) \left( \frac{1}{E_f' h_f} + \frac{1}{E_s' h_s} \right)^2 + 6 \left( \frac{1}{E_f' h_f^3} + \frac{1}{E_s' h_s^3} \right) \frac{h_a}{G_a}} \quad (9)$$

and  $\nu_a$  is the Poisson's ratio of the adhesive layer.

The maximum tensile stress in silicon films, which causes films to fracture, occurs at the center of the top surface, and is given by<sup>[25,26]</sup>

$$\sigma_{\text{crack}} = \left\{ G_a h_s \left[ \beta \left( \frac{2\chi^4}{\lambda^3} + \frac{\lambda}{2} \right) - \frac{2h_f \chi^4}{3\lambda^2} \right] + E_a' \right\} \times \frac{3\pi}{\chi^4 h_f^2 h_a L} \sqrt{\frac{dL}{L} - \frac{\pi^2 h_s^2}{12L^2}} \quad (10)$$

In fact, the surface strain of the film shown in Figure 9 is given by  $\sigma_{\text{crack}}/E_f'$

**Table 1.** Critical applied strain of each failure modes as the Si ribbons thickness on plastic substrate coated with adhesive layer.

Adhesive layer	epoxy(1.0 $\mu\text{m}$ )					
Substrate thickness ( $\mu\text{m}$ )	175	50	50	50	50	50
Si thickness (nm)	100	290	700	1,250	2,500	10,000
Fracture mode	crack	slipping	slipping	slipping	slipping+delamination	delamination
Applied strain ( $dL/L$ , %)	42.4	23.7	9.0	5.9	3.4/53.4	2.6
Nominal bend radius (mm)	2.88	3.86	6.26	7.73	10.2/2.57	11.6

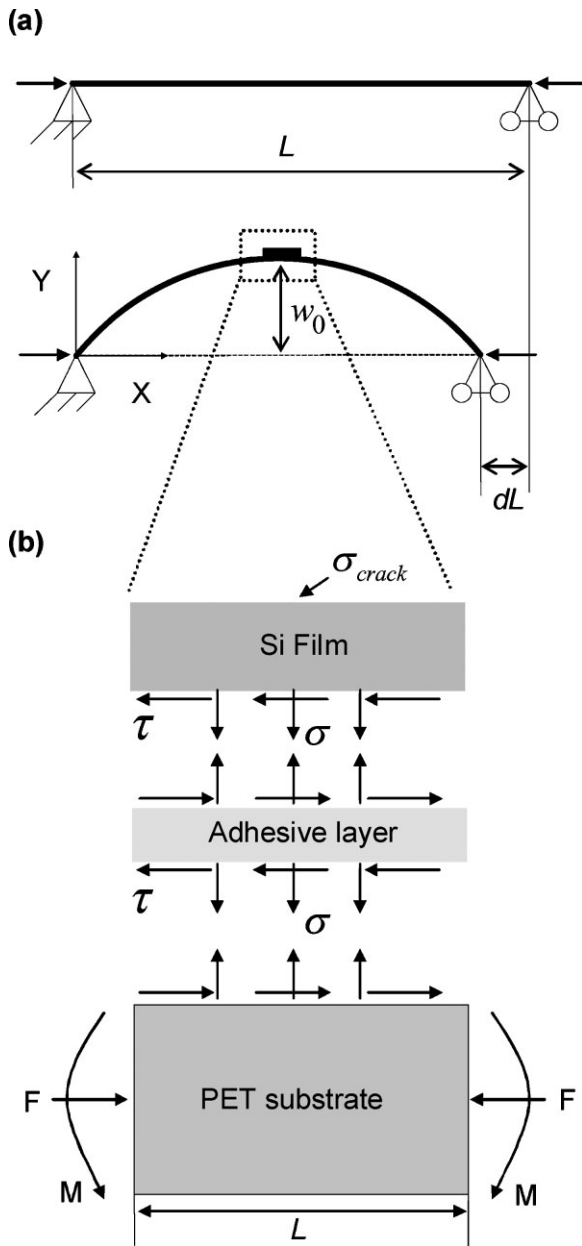


**Figure 8.** a) Coordinate system of post-buckling analysis as a beam b) stress analysis for a system composed of a thin film, adhesive layer and substrate subjected to the axial compressive force  $F$  and bending moment  $M = F w_0$ .

The interface slip occurs when the maximum interfacial shear stress in Equation 5 reaches the shear strength  $\tau_c$  of the interface, i.e.,

$$\tau_{\max} = \tau_c \quad (11)$$

For the 700 nm thick silicon film (and 1  $\mu\text{m}$  thick epoxy adhesive layer and 50  $\mu\text{m}$  thick PET substrate), the interfacial slip occurs at  $dL/L = 9.0\%$ . Equations 1, 5 and 11 give the

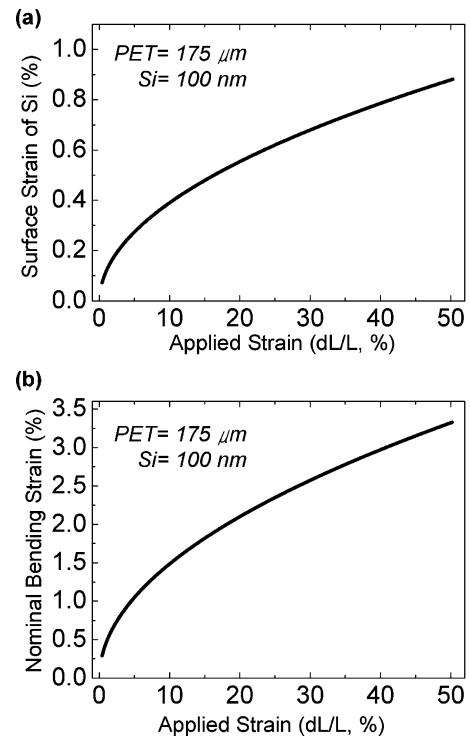


**Figure 9.** a) Surface strain in a silicon film; and b) nominal bending strain of PET substrate versus the applied strain  $dL/L$  for the 100 nm thick Si film, 1  $\mu\text{m}$  thick epoxy adhesive layer and 175  $\mu\text{m}$  thick PET substrate. The substrate a 175  $\mu\text{m}$  thick film of PET and an epoxy adhesive (Si ribbons: thickness = 100 nm,  $W/L = 20/500 \mu\text{m}$ ).

interfacial shear strength  $\tau_c = 20.8 \text{ MPa}$ , where the elastic properties of the film, adhesive layer and substrate are  $E_f = 130 \text{ GPa}$ ,  $\nu_f = 0.27$ ,  $E_a = 4.4 \text{ GPa}$ ,  $\nu_a = 0.44$ ,  $E_s = 4.0 \text{ GPa}$ , and  $\nu_s = 0.44$ .<sup>[27,28]</sup> Similarly, the interface delamination and film fracture occur when the maximum interfacial tensile (peeling) stress in Equation 7 and tensile stress in Equation 10 reach the tensile strengths  $\sigma_c$  of the interface and  $\sigma_c^{\text{Si}}$  of the silicon film, respectively, i.e.,

$$\sigma_{\max} = \sigma_c \quad (12)$$

$$\sigma_{\text{crack}} = \sigma_c^{\text{Si}} \quad (13)$$

For the 10  $\mu\text{m}$  thick silicon film (and 1  $\mu\text{m}$  thick epoxy adhesive layer and 50  $\mu\text{m}$  thick PET substrate), the interfacial delamination occurs at  $dL/L = 2.2\%$ . Equations 1, 7 and 12 give the interfacial tensile strength  $\sigma_c = 17.2 \text{ MPa}$ . For the 100 nm thick silicon film (and 1  $\mu\text{m}$  thick epoxy adhesive layer and 175  $\mu\text{m}$  thick PET substrate), the silicon film fractures at  $dL/L = 42.4\%$ , and Equations 1, 10 and 13 give the strength of silicon film  $\sigma_c^{\text{Si}} = 1.0 \text{ GPa}$ .

Figure 10 shows that the maximum interfacial shear and peeling stresses and film stress normalized by their corresponding strengths,  $\tau_{\max}/\tau_c$ ,  $\sigma_{\max}/\sigma_c$ , and  $\sigma_{\text{crack}}/\sigma_c^{\text{Si}}$ , as a function of silicon film thickness, for 50  $\mu\text{m}$  thick PET substrate. The

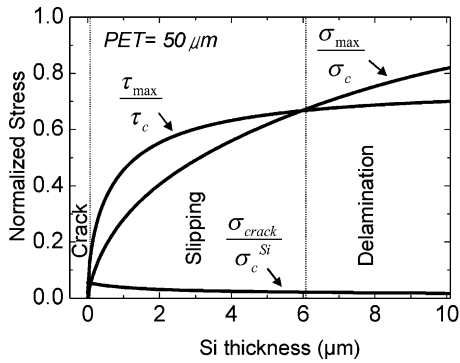
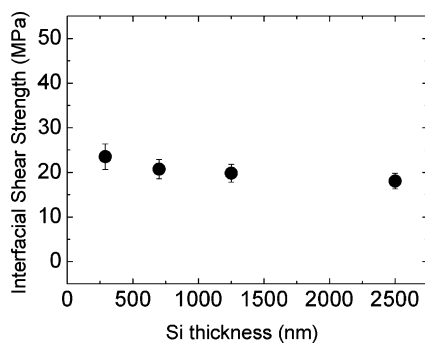


**Figure 10.** The stress to strength ratio versus the Si film thickness, which shows three failure mechanisms, namely the film cracking, interface slip, and interface delamination.

thickness of the adhesive layer is 1 μm, and the applied strain is  $dL/L = 1.5\%$ . For each film thickness, the stress ratios  $\tau_{\max}/\tau_c$ ,  $\sigma_{\max}/\sigma_c$ , and  $\sigma_{\text{crack}}/\sigma_c^{\text{Si}}$  all increase with  $dL/L$ , and whichever reaches unity first causes the corresponding failure. Figure 10 suggests the film cracking and interfacial delamination for film thickness below 17 nm and above 6.2 μm, respectively, and interfacial slip for film thickness between 17 nm and 6.2 μm. This ribbon-thickness dependence of failure modes is consistent with experimental results in the prior section. It is important to point out that different failure modes depend on the film, adhesive layer and substrate properties, but not on the applied strain  $dL/L$  because all stress ratios are proportional to

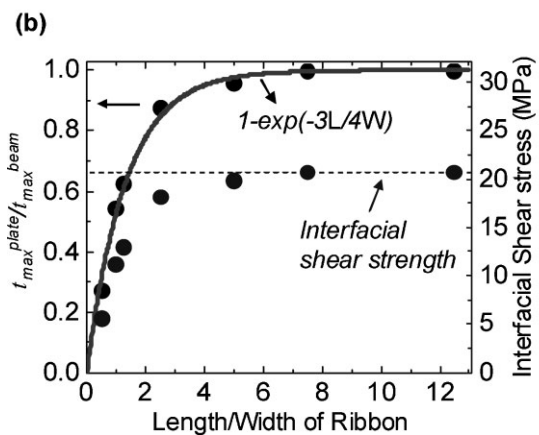
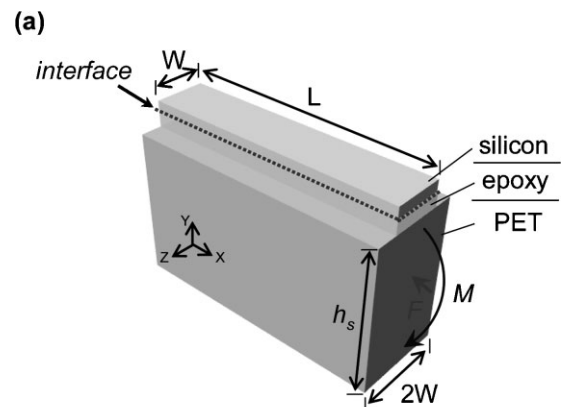
$$\sqrt{\frac{dL}{L}} - \frac{\pi^2 h_s^2}{12L^2}.$$

Figure 11 shows the interfacial shear strength  $\tau_c$  determined from the critical applied bending strain  $dL/L$  for interfacial slip measured from experiments at different film thickness. The interfacial shear strength is essentially independent of the film thickness, and is indeed a material property.



**Figure 11.** The interfacial shear strength determined from the slip of Si thin films with different thickness; the interfacial shear strength is essentially a constant ( $\tau_c = (20.7 \pm 2.2)$  MPa).

The above analysis is based on the beam theory, and therefore holds for the length  $L$  of silicon film much larger than the width  $W$ , for which the interfacial shear stress traction is mainly parallel to the ribbon direction. In most device configurations in electronics, the widths are comparable to the lengths, and therefore cannot be modeled as beams anymore since the interfacial shear stress tractions parallel and normal to the ribbon direction are on the same order. We have used the finite element method to study the maximum interfacial shear stress, denoted by  $\tau_{\max}^{\text{plate}}$ . Here the superscript “plate” is used to distinguish from the maximum interfacial shear stress in Equation 5 from the beam theory, and the latter is now denoted by  $\tau_{\max}^{\text{beam}}$ . Figure 12a shows the three-dimensional model for the finite element analysis. The numerical results suggest that the stress ratio  $\tau_{\max}^{\text{plate}}/\tau_{\max}^{\text{beam}}$  is approximately a universal function that depends only on the ribbon length to width ratio,  $L/W$ , and is independent of material properties and thickness. The stress ratio  $\tau_{\max}^{\text{plate}}/\tau_{\max}^{\text{beam}}$  is



**Figure 12.** The length effect of Si ribbons on an epoxy (~1 μm)/PET (50 μm) substrate; a) the model in the finite element analysis; b) the maximum interfacial shear stress  $\tau_{\max}^{\text{plate}}$  obtained from the finite element analysis, and its ratio to the maximum shear stress  $\tau_{\max}^{\text{beam}}$  given by the beam theory, versus the ribbon length to width ratio,  $L/W$ .

shown versus the ribbon length to width ratio  $L/W$  in Figure 12b, which can be well approximated by

$$\frac{\tau_{\max}^{\text{plate}}}{\tau_{\max}^{\text{beam}}} = 1 - \exp\left(-\frac{3L}{4W}\right). \quad (14)$$

This suggests that the ribbon length has essentially no effects (within 5% difference) for the ribbon length  $L$  four times larger than the width  $W$ . For  $L < 4W$ , the maximum interfacial shear stress decreases with the film length  $L$ , which agrees with the experiments reported in the previous section. This stress ratio decreases to about one half for the ribbon length equal to width,  $L = W$ . The combination of Equations 11 and 14 gives

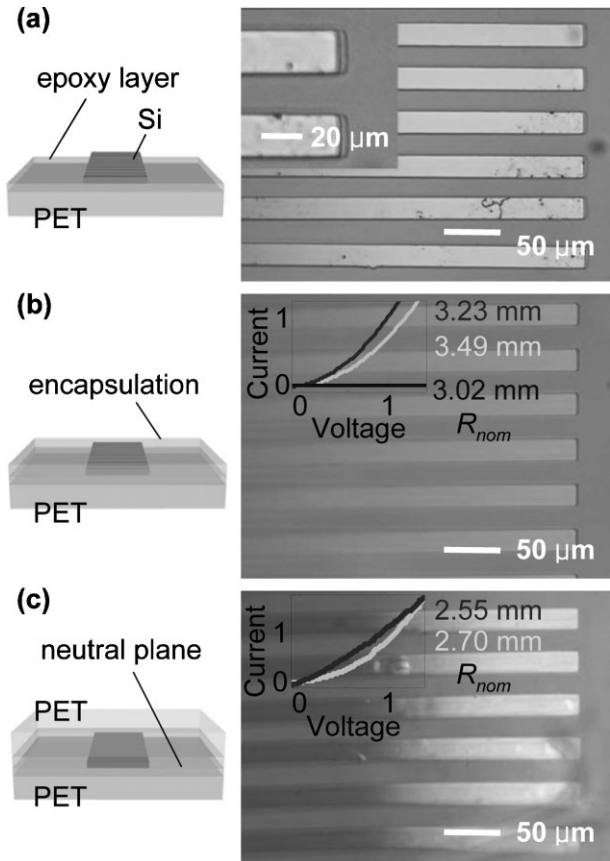
$$\tau_{\max}^{\text{plate}} = \frac{\pi h_s}{2L} \sqrt{\frac{G_a}{h_a \left( \frac{1}{E_j h_j} + \frac{1}{E_s h_s} \right)}} \sqrt{\frac{dL}{L} - \frac{\pi^2 h_s^2}{12L^2}} \left[ 1 - \exp\left(-\frac{3L}{4W}\right) \right]. \quad (15)$$

Figure 12b also shows the interfacial shear stress  $\tau_{\max}^{\text{plate}}$  versus the ribbon length to width ratio  $L/W$ . The applied strain  $dL/L$  (9.0%) is chosen such that the interface shear stress for long ribbons (thickness = 700 nm, width = 20  $\mu\text{m}$ , length = 500  $\mu\text{m}$ ) on an epoxy (~1  $\mu\text{m}$ )/PET (50  $\mu\text{m}$ ) substrate with length  $L = 11.8$  mm just reaches the interfacial shear strength  $\tau_c$ , which is marked by the dashed line in Figure 12b. For the same applied strain  $dL/L$ , the interfacial shear stress for short ribbons clearly falls short of the interfacial shear strength  $\tau_c$ .

The above analysis in this section holds for outward bending illustrated in Figure 8a. For inward bending (buckling in the opposite direction), the bending moment changes the sign,  $M = -F w_0$ . The interfacial shear stress also changes the sign, but its maximum remains the same as Equation 5, and therefore gives the same  $\tau_{\max}/\tau_c$  curve as Figure 10. The maximum interfacial peeling stress in Equation 7 becomes compressive for inward bending. The interfacial peeling stress for inward bending reaches maximum at a distance away from the free edge, and the maximum is only a small fraction of Equation 7.<sup>[25,26]</sup> Therefore the  $\sigma_{\max}/\sigma_c$  curve in Figure 10 is much lower for inward bending, and consequently the interface slipping becomes the dominant failure mode. This is, in fact, consistent with our experiments which show interface slipping for both 700 nm and 10  $\mu\text{m}$  thick PET substrate.

## 2.6. Other Implementations of the Concepts

Additional simple design modifications can improve the behavior beyond that described above. Figure 13 illustrates two methods, with comparison to an unoptimized system (Fig. 13a) after bending beyond the slipping failure mode. The unoptimized case corresponds to silicon ribbons with 290 nm thickness, 20  $\mu\text{m}$  widths and 500  $\mu\text{m}$  lengths on PET sheet (175  $\mu\text{m}$  thick) with length  $L = 12.0$  mm, coated with an epoxy layer (1  $\mu\text{m}$  thick). (To observe the slipping mode with an optical microscope, the epoxy layer was postbaked after



**Figure 13.** Optical images of a) uncovered Si ribbons on the plastic substrate during bending ( $dL/L = 30.8\%$ ,  $R_{\text{nom}} \sim 3.44$  mm;  $\epsilon_{\text{nom}} \sim 2.54\%$ ) beyond the slipping failure mode, b) encapsulated Si ribbons by epoxy with 2.5  $\mu\text{m}$  thickness during bending ( $dL/L = 35.8\%$ ,  $R_{\text{nom}} \sim 3.19$  mm;  $\epsilon_{\text{nom}} \sim 2.74\%$ ), and c) Si ribbons on neutral mechanical plane made by PET and epoxy of the same thickness with bottom substrate during bending ( $dL/L = 57.8\%$ ,  $R_{\text{nom}} \sim 2.51$  mm). The substrate shown in these images is a 175  $\mu\text{m}$  thick film of PET and an epoxy adhesive (~1  $\mu\text{m}$ ). The insets show a) optical image of a magnification of the slipping region and the current ( $\mu\text{A}/\text{ribbons}$ )–voltage (V) response of Si ribbon based simple p-n junction diodes with b) encapsulation layer and c) neutral mechanical plane layout.

printing the ribbons. In this manner, a slight indentation appears in the epoxy, which can be observed by optical microscopy.) Figure 13a shows an optical image of these silicon ribbons during bending of  $dL/L = 30.8\%$  ( $R_{\text{nom}} \sim 3.44$  mm;  $\epsilon_{\text{nom}} \sim 2.54\%$ ) which is much larger than that needed to initiate the slipping failure mode. The inset of Figure 13a provides a magnified view of the slipping region. By adding a thin, mechanically tough encapsulating layer on top of the inorganic layers, it is possible to increase both  $\tau_c$  and  $\sigma_c$ . Figure 13b, which shows an optical image of the silicon ribbons during bending of  $dL/L = 35.8\%$  ( $R_{\text{nom}} \sim 3.19$  mm;  $\epsilon_{\text{nom}} \sim 2.74\%$ ), illustrates an example of this strategy using a ~2.5  $\mu\text{m}$  thick layer of epoxy spin cast on top of Si ribbons, with other features of the system the same as those in Figure 13a. The inset of Figure 13b shows the current ( $\mu\text{A}/\text{ribbons}$ )–voltage (V) response of diodes covered by the encapsulation layer with other parameters the same as those in Figure 7a. The diode

operates up to  $dL/L = 35.0\%$  ( $R_{\text{nom}} \sim 3.23$  mm;  $\varepsilon_{\text{nom}} \sim 2.71\%$ ), but ceases to operate at  $dL/L = 40.0\%$  ( $R_{\text{nom}} \sim 3.02$  mm;  $\varepsilon_{\text{nom}} \sim 2.90\%$ ), due to slipping induced fracture of the metal at the silicon edge.

Neutral mechanical plane concepts that involve the addition of PET and epoxy on top of the Si/epoxy/PET substrate, can be used as a further optimization. Figure 13c illustrates this type of layout (i.e., PET/epoxy/Si/epoxy/PET) and an optical image of Si ribbons during bending of  $dL/L = 57.8\%$  ( $R_{\text{nom}} \sim 2.51$  mm). The image shows that the Si ribbons are stable without any failure at  $dL/L$  values that substantially exceed those associated not only with the slipping mode but also with cracking in the corresponding system without the PET/epoxy overlayers. These data are consistent with the ability of neutral mechanical plane concepts to provide high resistance to bend induce failure. The inset of Figure 13c shows the current ( $\mu\text{A}/\text{ribbons}$ )–voltage (V) response of p-n junction diodes in neutral mechanical plane layouts with other parameters the same as those in Figure 7a. In this layout, the current still flows through the diode at much higher degree of bending ( $dL/L = 50.0\%$  and  $56.0\%$ ;  $R_{\text{nom}} \sim 2.55$  mm and  $R_{\text{nom}} \sim 2.70$  mm) compared to the unoptimized system.

### 3. Conclusions

The results presented here show that thin layers of silicon weakly bonded to plastic substrates exhibit three different failure modes at sufficiently high bending strains: cracking, slipping, and delamination, depending on the silicon thickness. These failure modes are controlled by surface strain, interfacial shear stress, and interfacial normal stress, respectively. Experimental data agree well with analytical modeling based on beam theory. We further demonstrated that the lateral dimensions (i.e., the lengths) of the Si ribbons are important, as quantitatively verified by analytical modeling based on plate theory. In particular, smaller regions of Si lead to more robust bending properties. The addition of encapsulating layers or neutral mechanical plane layouts can further improve bendability. These guidelines can be important for the design of flexible electronic systems that involve not only silicon but all classes of inorganic materials on plastic substrates.

### 4. Experimental

**Fabrication of Silicon Ribbons on Plastic Substrates:** Photoresist (PR; AZ 5214, 3000 rpm, 30 s) was coated on a silicon-on-insulator (SOI) wafer (Soitec or Shin-Etsu) and baked at  $110^\circ\text{C}$  for 1 min. This layer of PR was then photolithographically exposed ( $10\text{ mWcm}^{-2}$ , 12 s, Karl Suss MJB3 mask aligner) and developed (AZ 327 MIF developer, 45 s) to define the layouts of the Si ribbons. Dry etching using  $\text{SF}_6$  reactive gas (Plasma-Therm reactive ion etching (RIE) system, 40 sccm, 50 mTorr, 100 W) through the PR etched the exposed silicon to expose the buried oxide. SOI wafers with  $10\ \mu\text{m}$  thick top Si layer were etched with a  $\text{SF}_6/\text{O}_2$  inductively coupled plasma reactive ion etching system (STS-ICPRIE, STS Mesc Multiplex Advanced Silicon

Etcher) through a patterned layer of  $\text{Si}_3\text{N}_4/\text{SiO}_2$  (3/30 nm), as a hard mask, grown by plasma enhanced chemical vapor deposition (PECVD, Plasma-Therm) and patterned by photolithography and etching. After removing the PR with acetone, undercut etching of the buried oxide was performed with concentrated hydrofluoric (HF) acid solution ( $\sim 49\text{ wt}\%$  in water). The hard mask for the  $10\ \mu\text{m}$  thick Si layer was also removed by HF. The Si ribbons sagged to bottom Si handle wafer at the end of this etching process. To pick the ribbons up from the wafer, a flat elastomeric stamp of polydimethylsiloxane (PDMS) (Sylgard 184, Dow Corning) contacted the Si ribbons on the wafer after blow drying with  $\text{N}_2$  gas. The ribbons adhered to PDMS by Van der Waals interactions.

The target substrate consisted of a sheet of poly(ethyleneterephthalate) (PET) ( $50\ \mu\text{m}$ ,  $175\ \mu\text{m}$  in thickness, Glafix Plastics) spin-coated with a thin adhesive layer ( $\sim 1\ \mu\text{m}$ ). This adhesive consisted of an epoxy (SU8, Microchem Corp.) film, spin-coated (75% diluted solution, 3000 rpm, 40 s) and cured at  $65^\circ\text{C}$  and  $110^\circ\text{C}$  for 1 min each, exposed to UV light ( $10\text{ mWcm}^{-2}$ , 12 s), and then postbaked at  $115^\circ\text{C}$  for 1.5 min to induce cross-linking.

The transfer of the Si ribbons from PDMS stamp to plastic substrate was accomplished by contacting the stamp, coated with Si ribbons, against the PET substrate with a thin adhesive layer and then removing the stamp. Removal was performed at slow speeds by use of heating ( $110^\circ\text{C}$ , 1.5 min), to induce thermal expansion in the PDMS and, in this way, to initiate separation of the PDMS stamp and the ribbons. After the transfer, the Si/epoxy/PET substrate was baked at  $110^\circ\text{C}$  for 13.5 min on a hot plate to complete removal of solvent and the cure.

**Device Fabrication:** Simple p-n junction diodes were formed using Si ribbons (290 nm) doped with high concentration of phosphorous (n-type,  $\sim 10^{19}\text{ cm}^{-3}$ ) on one side and low concentration of boron (p-type,  $6.0\text{--}9.4 \times 10^{14}\text{ cm}^{-3}$ ) on the other. The n-type region was defined by spin casting a phosphorus containing spin-on dopant (Filmtronic) and then performing rapid thermal annealing (RTA,  $950^\circ\text{C}$ , 5 s) to induce diffusion of the dopant. The p-type region was provided by the pre-existing doping level of the SOI wafers obtained from the vendor. The Si ribbons with p-n doped regions formed in this manner were transferred to plastic, as described in previous paragraph. Metal layers of Ti/Au (thickness =  $5/70$  nm), deposited by electron beam evaporation and patterned by liftoff through a photolithographically patterned layer of photoresist (AZ5214) provided electrical contacts. This metal covered the end parts of the silicon, the end edges of the silicon and the adjacent plastic substrate. The devices were probed by making contacts to the metal on the plastic.

**Bending test:** We observed the silicon during bending using optical microscopy and through the SEM, (Philips XL30 ESEM-FEG) at tilt angles (outward bending:  $38.5^\circ$ , inward bending:  $\sim 30^\circ$ ) and 1 keV operating voltages. A home-built set of translation stages capable of mounting directly in the SEM was used for viewing during the bending process. The measurements were performed with the ribbons on substrates with initial length  $L$ , subject to compression with external force applied through the bending stage. The plastic substrate bent to an end-to-end length of  $L - dL$  in a horizontal distance from one edge of the bent substrate to the other. The setups allow the length to be measured with an accuracy better than  $\sim 0.1$  mm, with continuous control of  $L - dL$ , in increments of  $\sim 0.1$  mm.

Received: March 2, 2008

Revised: April 30, 2008

Published online: September 1, 2008

- [1] R. H. Reuss, B. R. Chalamala, A. Moussessian, M. G. Kane, A. Kumar, D. C. Zhang, J. A. Rogers, M. Hatalis, D. Temple, G. Modell, B. J. Eliasson, M. J. Estes, J. Kunze, E. S. Handy, E. S. Harmon, D. B. Salzman, J. M. Woodall, M. A. Alam, J. Y. Murthy, S. C. Jacobsen,

- M. Oliver, D. Markus, P. M. Campbell, E. Snow, *Proc. IEEE* **2005**, *93*, 1239.
- [2] J. A. Rogers, Z. Bao, K. Baldwin, A. Dodabalapur, B. Crone, V. R. Raju, V. Kuck, H. Katz, K. Amundson, J. Ewing, P. Drzaic, *Proc. Natl. Acad. Sci. USA* **2001**, *98*, 4835.
- [3] T. Someya, T. Sekitani, S. Iba, Y. Kato, H. Kawaguchi, T. Sakurai, *Proc. Natl. Acad. Sci. USA* **2004**, *101*, 9966.
- [4] C. Reese, Z. Bao, *Mater. Today* **2007**, *10*, 20.
- [5] S. R. Forrest, *Nature* **2004**, *428*, 911.
- [6] W. S. Wong, S. Ready, R. Matusiak, S. D. White, J.-P. Lu, R. Lau, J. Ho, R. A. Street, *Mater. Res. Soc. Symp. Proc.* **2001**, *664*, A17.4.1.
- [7] Y. Sun, J. A. Rogers, *Adv. Mater.* **2007**, *19*, 1897.
- [8] M. C. McAlpine, R. S. Friedman, S. Jin, K.-H. Lin, W. U. Wang, C. M. Lieber, *Nano Lett.* **2003**, *3*, 1531.
- [9] D. V. Talapin, C. B. Murray, *Science* **2005**, *310*, 86.
- [10] H.-C. Yuan, Z. Ma, *Appl. Phys. Lett.* **2006**, *89*, 212105.
- [11] S. A. Scott, M. G. Lagally, *J. Phys. D* **2007**, *40*, R75.
- [12] S. Ju, A. Facchetti, Y. Xuan, J. Liu, F. Ishikawa, P. Ye, C. Zhou, T. J. Marks, D. B. Janes, *Nat. Nanotechnol.* **2007**, *2*, 378.
- [13] L. Wang, M.-H. Yoon, A. Facchetti, T. J. Marks, *Adv. Mater.* **2007**, *19*, 3252.
- [14] H. Gleskova, S. Wagner, Z. Suo, *Appl. Phys. Lett.* **1999**, *75*, 3011.
- [15] H. Gleskova, S. Wagner, Z. Suo, *J. Non-Cryst. Solids* **2000**, *266-269*, 1320.
- [16] A. J. Baca, J.-H. Ahn, Y. Sun, M. Meitl, E. Menard, H.-S. Kim, W.-M. Choi, D.-H. Kim, Y. Huang, J. A. Rogers, *Angew. Chem. Int. Ed.*, in press.
- [17] Y.-L. Loo, T. Someya, K. W. Baldwin, Z. Bao, P. Ho, A. Dodabalapur, H. E. Katz, J. A. Rogers, *Proc. Natl. Acad. Sci. USA* **2002**, *99*, 10252.
- [18] S. P. Lacour, J. Jones, S. Wagner, T. Li, Z. Suo, *Proc. IEEE* **2005**, *93*, 1459.
- [19] D.-H. Kim, J.-H. Ahn, W.-M. Choi, H.-S. Kim, T.-H. Kim, J. Song, Y. Huang, Z. Liu, C. Lu, J. A. Rogers, *Science* **2008**, *320*, 507.
- [20] Y. Sun, W. M. Choi, H. Jiang, Y. Huang, J. A. Rogers, *Nat. Nanotechnol.* **2006**, *1*, 201.
- [21] Z. Suo, E. Y. Ma, H. Gleskova, S. Wagner, *Appl. Phys. Lett.* **1999**, *74*, 1177.
- [22] H. C. Ko, A. Baca, J. A. Rogers, *Nano Lett.* **2006**, *6*, 2318.
- [23] M. A. Meitl, Z.-T. Zhu, V. Kumar, K. J. Lee, X. Feng, Y. Huang, I. Adesida, R. G. Nuzzo, J. A. Rogers, *Nat. Mater.* **2006**, *5*, 33.
- [24] S. P. Timoshenko, J. M. Gere, in *Theory of Elastic Stability*, 2nd ed., McGraw Hill, New York **1961**, Ch. 2 and 9.
- [25] Z. Q. Jiang, Y. Huang, A. Chandra, *J. Electron. Packag.* **1997**, *119*, 127.
- [26] K. P. Wang, Y. Huang, A. Chandra, K. X. Hu, *IEEE Trans. Compon. Packag. Technol.* **2000**, *23*, 309.
- [27] K. Kim, E. Nilsen, T. Huang, A. Kim, M. Ellis, G. Skidmore, J.-B. Lee, *Microsyst. Technol.* **2004**, *10*, 689.
- [28] B. L. Weick, B. Bhushan, *IEEE Trans. Magn.* **1996**, *32*, 3319.